Enabling Hyperspectral Imaging in Diverse Illumination Conditions for Indoor Applications

by

Puria Azadi Moghadam

B.Sc., University of Tehran, 2019

Thesis Submitted in Partial Fulfillment of the
Requirements for the Degree of
Master of Science

in the
School of Computing Science
Faculty of Applied Sciences

SIMON FRASER UNIVERSITY
Summer 2021

Declaration of Committee

Name: **Puria Azadi Moghadam**

Degree: **Master of Science (Computing Science)**

Title: **Enabling Hyperspectral Imaging in Diverse Illumination Conditions for Indoor Applications**

Committee: **Chair:** Ouldooz Baghban Karimi
Limited-Term Lecturer, Computing Science

Mohamed Hefeeda
Supervisor
Professor, Computing Science

Khaled Diab
Committee Member
University Research Associate, Computing Science

Shervin Shirmohammadi
Examiner
Adjunct Professor, Computing Science

Abstract

Hyperspectral imaging provides rich information across many wavelengths of the captured scene, which is useful for many potential applications such as food quality inspection, medical diagnosis, material identification, artwork authentication, and crime scene analysis. However, hyperspectral imaging has not been widely deployed for such indoor applications. In this work, we address one of the main challenges stifling this wide adoption, which is the strict illumination requirements for hyperspectral cameras. Hyperspectral cameras require a light source that radiates power across a wide range of the electromagnetic spectrum. Such light sources are expensive to setup and operate, and in some cases, they are not possible to use because they could damage important objects in the scene. We propose a deep-learning method that enables indoor hyperspectral imaging using cost-effective and widely available lighting sources such as LED and fluorescent. These common sources, however, introduce significant noise in the hyperspectral bands in the invisible range, which are the most important for the applications. Our proposed method restores the damaged bands using a deep-learning model. We conduct an extensive experimental study to analyze the performance of the proposed method and compare it against the state-of-the-art using real hyperspectral datasets that we have collected. Our results show that the proposed method outperforms the state-of-the-art across all considered objective and subjective metrics, and it produces hyperspectral bands that are close to the ground truth bands captured under ideal illumination conditions.

Keywords: Hyperspectral Imaging, Deep Learning

Dedication

To mom and dad, who have always been there for me; and to my brother, my best friend.
God bless you all.

Acknowledgements

I would like to state my sincere gratitude to my supervisor Dr. Hefeeda for his unremitting support during this path. Also, I would like to thank Neha Sharma who has been very helpful in the project. Finally, I am also thankful to the committee members, Dr. Baghban Karimi as the chair, Dr. Diab as supervisor, and Dr. Shirmohammadi as examiner.

Table of Contents

List of Tables

List of Figures

Chapter 1

Introduction

This chapter starts by giving an overview about hyperspectral imaging and its usages. Then it states the considered problem in the thesis and summarizes our contributions.

1.1 Hyperspectral Imaging

A regular camera captures a scene in the visible range of the light spectrum through three main wavelengths: Red (R), Blue (B), and Green (G). These wavelengths were chosen based on the characteristics of the human visual system and its sensitivities to different colors. In contrast, a hyperspectral camera captures a scene in many wavelengths across a wide range of the spectrum, including bands invisible to humans such as the infrared (IR) band. Thus, hyperspectral cameras offer very rich information about the captured scene, which enables deeper understanding of various objects in the scene, even if they are not visible to the human eye. A sample hyperspectral band is shown in Figure 1.1. Notice that the internal defects of the avocado that cannot be seen in the RGB image appear in the shown 830nm, IR, band.

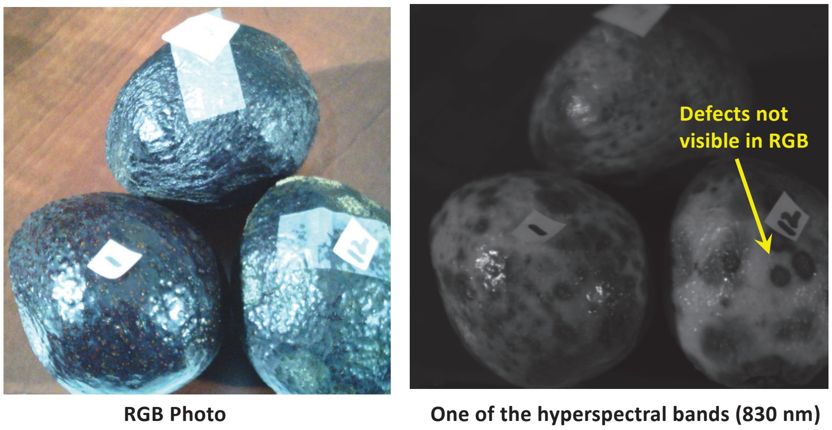

Figure 1.1: RGB versus hyperspectral images.

Hyperspectral imaging has been used in various industrial and military applications including remote sensing, surveillance, identification of camouflaged objects, agricultural research, forest monitoring, pollution monitoring, among many others [35, 5, 42, 21]. Many of the commercially deployed hyperspectral imaging systems are large-scale and mostly deployed in outdoor environments. In addition, the potential of hyperspectral imaging has been demonstrated in indoor applications including medical diagnosis (e.g., early detection of skin cancer), food quality inspection (e.g., determining the ripeness of fruits and fat content in meats), artwork authentication, and material identification[2, 37, 27, 8, 41]

1.2 Problem Statement

Indoor illumination refers to a condition, which the scene is illuminated by artificial light sources and they do not cover all the electromagnetic spectrum. However, sunlight with wide spectral power distribution mainly exists in outdoor illumination conditions. Hyperspectral imaging has not seen wide deployment in indoor applications yet, because of the cost and complexity associated with setting up hyperspectral imaging systems. One of the main challenges is the strict illumination requirements for current hyperspectral cameras to function properly. Specifically, since hyperspectral cameras capture bands in the visible and invisible range of the spectrum, they require a light source that radiates power across a wide range of the electromagnetic spectrum to illuminate the scene being captured. The current solution to address this requirement is to use halogen light sources, which cover a large part of the spectrum [13]. However, halogen light sources have limitations, which stifle the adaptation of hyperspectral imaging systems for indoor application. Souza et al. [9] performed an economic analysis based on the annualized lifetime cost of halogen incandescent, Compact Fluorescent Lamp (CFL), and Light-Emitting Diodes (LED) lamps by considering their costs of replacement, acquisition, energy consumption, and other expenses. Their study shows that for 5 hours of daily use, the annualized life cycle cost for halogen lamps is about 3.64 times higher than CFL cost and 4.73 times higher than LED cost.

Moreover, Nardelli et al. [30] analyzed the characteristics of 375 lamps of 6 various types including halogen, CFL, and LED bulb existing in the Brazilian, North American, and European markets. Their experiments indicate that the average lifetimes of LED and CFL are 10 times and 2.85 times longer than that of halogen lamps, respectively. Also, these two light sources provide higher lumens per watt than halogen lamps while they have a longer lifespan.

One of the other aspects of choosing light sources is their environmental effects. In 2009, OSRAM Photonics company, one of the globally leading brands in the light industry, introduced 6 categories for assessment of light sources' environmental impacts including Global Warming Potential (GWP), Acidification Potential (AP), Eutrophication Potential (EP), Photochemical Ozone Creation Potential (POCP), Human Toxicity Potential (HTP), and Abiotic Depletion Potential (ADP) [36]. Souza et al. [9] studied the life cycle environmental impacts of incandescent halogen, CFL, and LED illumination sources throughout manufacturing, use, and disposal phases and showed that halogen lamps have the highest effect compared to other two light sources in all the mentioned 6 categories. Contribution of various light sources is shown in Figure 1.2 based on the data presented in [9].

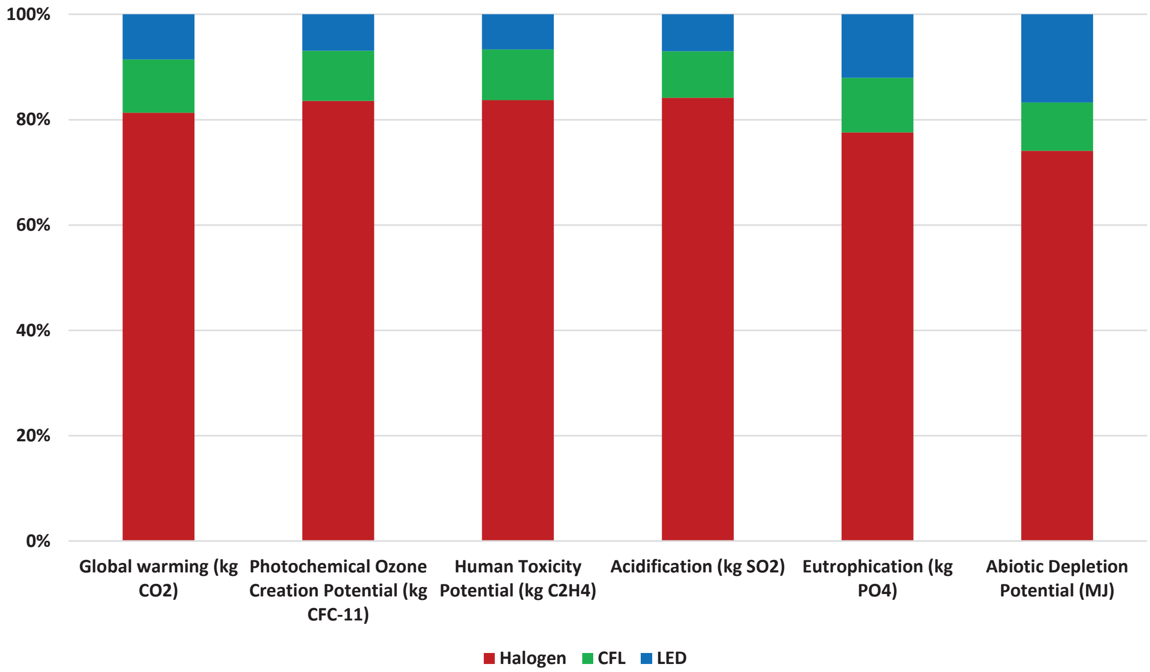

Figure 1.2: Comparison of environmental impacts of halogen, CFL, and LED lamps.

Energy efficiency for artificial light sources shows the conversion rate of electricity into luminous flux (lm/W). luminous flux, which is usually reported in lumens instead of watts and is measured by a goniophotometer [34]. Lower efficiency in electrical devices means a higher amount of wasted energy in form of heat. Nardelli et al. [30] surveyed the luminous efficiency of 379 illumination sources. Their analysis showed that CFL and LED have a close average luminous efficiency value (of about 60 lm/W) while power usage of most of examined LED and CFL lamps were less than 20 W and 50 W respectively. Also, the average efficiency of studied halogens was around 17 lm/W, and their power usages were mostly between 20 W to 70 W. Therefore, compared to CFL and LED illumination sources, halogen lamps have a considerably smaller value of energy efficiency while consuming a higher amount of electricity leading to releasing a significant amount of heat.

In summary, halogen light sources are expensive, have a short lifetime, consume substantial amounts of electricity, and in many cases, they are not available or even possible to use because they may alter the characteristics of objects in the captured scene due to the heat produced by these sources. For instance, hyperspectral imaging has been proposed for forensics and crime scene analysis in [11, 20], in which case even if halogen sources are possible to setup, they may affect the outcome of the analysis. Similarly, halogen light sources are not suitable for hyperspectral systems designed for artwork authentication [31], as they may damage the artwork, and food quality inspection [12, 46, 43], as they may spoil some food items or affect their ripeness.

The goal of this thesis is to enable indoor hyperspectral imaging using cost-effective and widely available lighting sources such as CFL and LED. This is a challenging problem since the common CFL and LED light sources emit low power in the invisible range of the spectrum. Hyperspectral images consist of rich information about the scene by providing spectral signature for each pixel. Major number of hyperspectral applications such as material identification relay heavily on spectral information in addition to spatial features, and they utilize unsupervised methods including clustering approaches [28] or supervised classification methods [26], which applied on spectral signatures features to analyze the scene. However, hyperspectral imaging in the indoor area under various illumination sources including CFL and LED causes significant damages in the wide domain of hyperspectral bands captured in the IR range by the camera, which are the most important bands for the applications. In addition, a higher amount of details needs to be recovered in indoor scenes compared to remote sensing applications, and it increases the difficultly of this problem.

1.3 Thesis Contributions

In this thesis, we propose a deep learning method to restore the damaged bands captured with LED and CFL light sources. The proposed method greatly facilitates the deployment of hyperspectral imaging systems for many real-life applications in a cost-effective and efficient manner.

The contributions of this thesis can be summarized as follows [3]:

- We conduct an empirical study to analyze the effects of different light sources on hyperspectral imaging. Unlike prior studies [22, 7], our study focuses on the impact of common light sources on the hyperspectral bands. Our analysis shows that the commonly used LED and CFL light sources introduce significant noises and damages in the hyperspectral bands in the invisible range of the spectrum.

- We propose a supervised deep learning model to restore the damaged hyperspectral bands. The proposed model considers both the spatial and spectral characteristics of hyperspectral images. It is also general as it can restore different number of hyperspectral bands.

- We collect a unique hyperspectral image dataset in this domain, which contains different objects and materials captured by a high-end hyperspectral camera using three different lighting sources: halogen, CFL, and LED. The dataset is available at [1].

- We conduct an extensive empirical study to analyze the performance of the proposed hyperspectral band restoration method and compare it against the closest work in the literature, using multiple objective and subjective metrics. Our results show that the proposed method outperforms the state-of-the-art across all metrics, and it produces hyperspectral bands that are close to the ground truth bands captured under ideal illumination conditions.
- We open source all our dataset and code. The work done in this thesis is based on our paper [3] which has received the reproducibility badge from the ACM Multimedia Systems 2021 Conference.

1.4 Thesis Organization

The rest of the thesis is organized as follows. We summarize the related work in Chapter 2. We analyze the illumination effects on hyperspectral imaging in Chapter 3 and describe the considered problem and our proposed solution in Chapter 4. In Chapter 5, we present our evaluation, and conclude the thesis in Chapter 6. In the appendix A, we describe the details of our dataset and code. We also explain how our research results can be fully reproduced by other researchers.

Chapter 2

Background and Related Work

This chapter first presents a brief background on hyperspectral imaging. Then, it summarizes the related works in the literature.

2.1 Background

Figure 2.1 illustrates the basic concepts behind hyperspectral imaging and how it is different from regular RGB imaging. The figure shows different parts of the electromagnetic spectrum. An RGB camera samples the spectrum in the visible range, which approximately lies between 400–700 nm. The RGB camera takes only three samples, centred around the red, green, and blue wavelengths. These three wavelengths were chosen based on the characteristics of the human visual system.

In contrast, a hyperspectral camera takes many more samples from the electromagnetic spectrum and goes beyond the visible range. Many of the hyperspectral cameras that are used for indoor applications capture bands from 400nm to 1000nm, and these bands are typically equally spaced in that range. For example, the Specim IQ camera used in our experiments captures 204 bands between 400nm and 1000nm, with a spectral resolution of $\sim$3nm. As shown in the lower part of Figure 2.1, this fine-grained sampling of the spectrum allows creating the so-called *spectral signatures*. A spectral signature shows how the reflectance (signal intensity) varies across different wavelengths. Recall that the reflectance of light (and its various wavelengths) depends on the material(s) of the surface that reflects the light. Thus, spectral signatures can be used to classify objects and identify their material composition.

In Figure 2.2, we show an example of spectral signatures. Two signatures are shown of different areas of an apple. Various methods of classification [26] and clustering [28] can be utilized to separate defective region from healthy one.

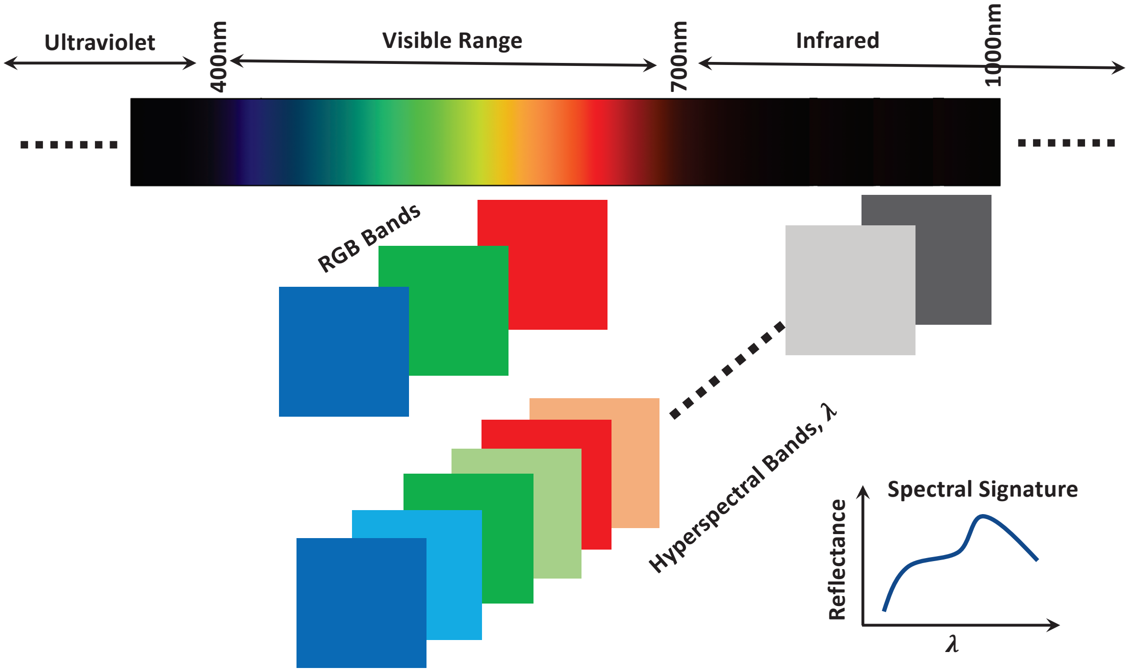

Figure 2.1: Basic concepts of hyperspectral imaging.

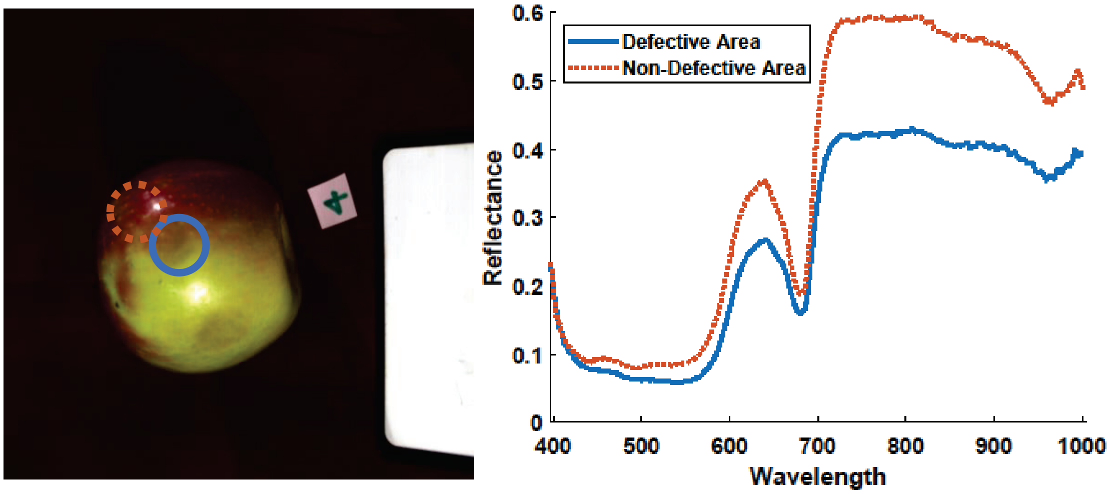

Figure 2.2: Spectral signatures of defective and non defective areas of an apple.

2.2 Related Work

Hyperspectral imaging has been getting popular in recent years, because of technological advances in the camera design as well as the introduction of powerful machine learning tools that can address long-standing problems in this domain. For example, multiple works have considered estimating hyperspectral bands from regular RGB images, e.g., [15, 18, 37]. Other works have proposed methods to up-sample multispectral (with few bands) images to hyperspectral images with many more bands and/or higher spatial resolutions, e.g., [16, 24]. Most of these works estimate bands in the visible range of the electromagnetic spectrum, which adds small value beyond RGB images for real-life hyperspectral imaging applications. In this thesis, we focus on maximizing the utility of images captured (not estimated) by hyperspectral cameras.

The quality of hyperspectral data can be affected during the acquisition process, because of various reasons such as weather and illumination conditions. Thus, multiple data enhancement methods have been proposed in the literature to increase the utility of hyperspectral images, which are expensive to collect. For example, Sidorov et al. [39] introduced the concept of the Deep Hyperspectral Prior, which is an extension of the Deep Image Prior [25], for enhancing hyperspectral images for indoor applications.

Prior works for enhancing hyperspectral images mostly consider mitigating noises in remote sensing images. In remote sensing applications, noises and artifacts are introduced because of atmospheric influences such as clouds, haze, rain, fog, and other weather conditions [33]. Such weather conditions do not impact indoor hyperspectral imaging applications. However, indoor applications may suffer from distortions and noises because of the illumination conditions. Specifically, outdoor hyperspectral applications benefit from the sunlight, which has a wide spectral power distribution covering most of the electromagnetic spectrum. Having an illumination source with wide spectral coverage is vital for capturing hyperspectral images, as many of the bands are not in the visible light range. To provide such wide spectral coverage for indoor applications, halogen light sources have typically been required. However, as mentioned in Chapter 1, halogen sources limit the adoption of hyperspectral imaging because they have short lifetimes and are expensive to operate and install, compared to the widely available light sources such as LED and CFL. LED and CFL light sources have low radiance intensities in the infrared (invisible) range; however, they were designed for everyday use. As shown later in this work, using LED and CFL light sources results in damaged hyperspectral bands, especially in the invisible range. This damage is different in nature from the effect of noise in outdoor applications. In outdoor applications, noise is added to the original signal, while in indoor applications, the signal is weak from the source because of the low radiance in the invisible range.

The closest work to ours is the recent work in [44]. It uses 3D convolutions and recurrent neural networks (RNN) to improve the quality of hyperspectral images, and was shown to outperform other works in the literature. We compare the performance of our proposed method against this work.

Chapter 3

Effect of Illumination on Hyperspectral Images

In this chapter, we analyze the impact of various types of lighting sources on hyperspectral images.

3.1 Effect of Illumination

Illumination plays a crucial role in capturing hyperspectral images. We start with some basics. To obtain a hyperspectral image, a light source illuminates the scene. Then, the reflected light from the scene is detected by the camera system, which divides it into wavelengths using a prism or grating structure, based on the camera design [4, 32]. Then, the various wavelengths are captured by the camera sensor to produce the hyperspectral bands.

Let us denote the observed image value at pixel (x, y) of the nth band as $I(x, y, \lambda_n)$. The light source intensity at the position of (x, y) is a function of the wavelength λ and is denoted by $L(x, y, \lambda)$. The surface reflectance is denoted by $S(x, y, \lambda)$ at the location (x, y), and the sensitivity function of the camera for the nth band is indicated by $C_n(\lambda)$. Then, the image value can be defined as follows [14]:

$$I(x, y, \lambda_n) = \int S(x, y, \lambda) \cdot L(x, y, \lambda) \cdot C_n(\lambda) \cdot d\lambda. \tag{3.1}$$

We note that $C_n(\lambda)$ is predetermined by the camera manufacturer, and the surface reflectance $S(x, y, \lambda)$ depends on the material composition of the objects in the scene. Thus, the illumination source and its intensity at different wavelengths directly impacts the values of the captured pixels of the hyperspectral image.

To capture hyperspectral images indoor, current systems require a light source that covers the 400–1,000 nm wavelength range with sufficient intensity. To meet this requirement, halogen light sources are typically used since such sources have wide spectral power density [45]. However, as described in Chapter 1, halogen light sources are expensive to setup and operate, not durable, and more importantly, they may alter or damage some objects in the scene.

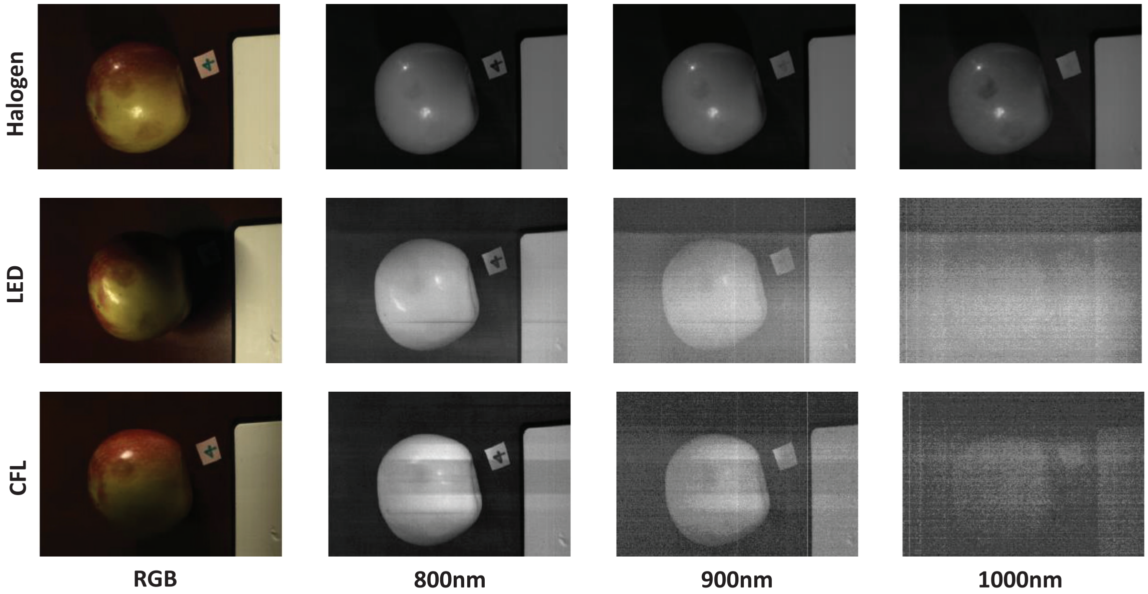

Figure 3.1: Effect of common illumination sources on capturing hyperspectral images of fruit samples.

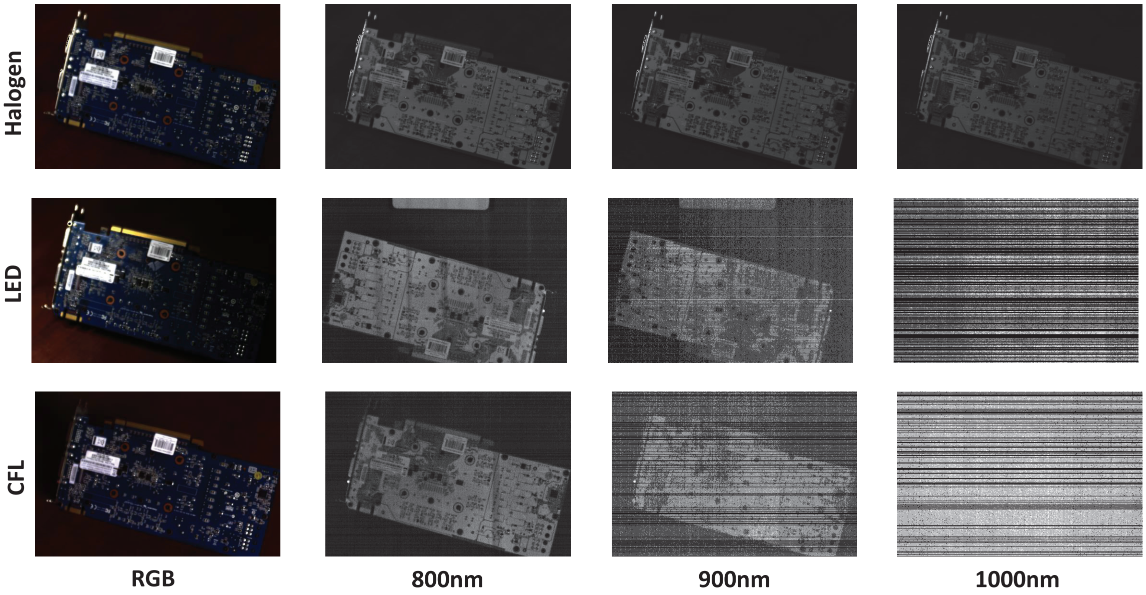

Figure 3.2: Effect of common illumination sources on capturing hyperspectral images of object samples.

LED and CFL light sources, on the other hand, are widely deployed, do not emit significant heat, and cost effective. However, these sources were designed to operate in the visible light range. Thus, the intensity of these sources beyond the 700 nm wavelength is low and

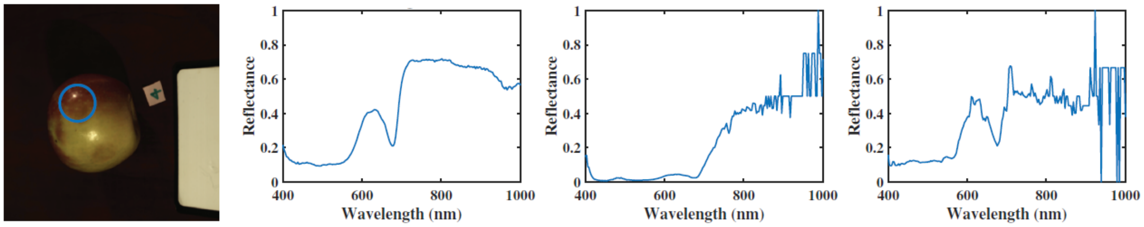

(a) RGB (b) Halogen (c) LED (d) CFL

Figure 3.3: Spectral signatures plotted for the area marked by the blue circle using three different light sources.

not uniform. This results in significant distortions in the hyperspectral bands captured in the 700–1,000 nm range, which are the most useful for hyperspectral applications as they contain information not visible to the human eyes and cannot be detected by other bands in the visible range. This is because bands in the 700–1,000 nm range belong to the near IR part of the spectrum, and they can penetrate surfaces and materials deeper than other bands.

We conducted multiple experiments to show the damaging effects of capturing hyperspectral images using LED and CFL sources, in contrast to halogen sources. Specifically, we used a high-end hyperspectral camera to capture various objects under halogen, LED, and CFL lighting conditions. The model of the hyperspectral camera is *Specim IQ*, and it captures 204 bands in the 400–1,000 nm range with a spectral resolution of ∼3nm. The objects captured include apples, avocados, and meat samples. Different types of fruits with different degrees of ripeness were used.

There are many models for LED, CFL, and halogen sources.[1] We selected one of the common models in the market for each of these three light sources. We note that each light source has its own unique characteristics, which all of its models share. The differences are usually in the color temperature and wattage. For example, all CFL sources function in the same way, regardless of their size and wattage, which is quite different from how LED and halogen function. Thus, although the three models used in the experiments do not cover all possible lighting conditions, they offer representative samples for LED, CFL, and halogen sources. The chosen models are: (i) 135-watt CFL source that emits 7600 luminous units (LM) and 5500K color temperature, (ii) 9-watt LED source with 1000 LM and 4000K color temperature, and (iii) 250-watt halogen source with 6050 LM and a 3050K color temperature.

We analyze the results along two aspects: captured bands and spectral signatures. A representative sample of our results is shown in Figures 3.1 and 3.3, for an apple with a small defect. In Figure 3.1, we show the RGB image as well as three hyperspectral bands

---

[1] The characteristics of more than 180 LED, CFL, and Halogen sources can be found at `https://lspdd.org/app/en/home`.

produced by the camera, under the three lighting sources. As the top row of the figure shows, the halogen source produces clear bands. Whereas the CFL source (middle row) and the LED source (bottom row) introduce a substantial amount of noise in the captured hyperspectral bands, especially as the bands get further away from the visible range. Note that bands that are in the IR range are the most useful for hyperspectral applications, and these are the ones that are damaged the most.

A closer look across the entire spectral range is shown in Figure 3.3 for a small area of the object, marked by the blue circle. We used the average value of the pixels in each band and plotted this value for each band. The spectral signatures shown in Figures 3.3.c and 3.3.d are produced using LED and CFL light sources, respectively, have significant fluctuations and noise compared to the cleaner signature in Figure 3.3.b, which is produced using the halogen source. Such fluctuations in the spectral signatures negatively impact the accuracy of the processing tasks performed on the captured hyperspectral images [10].

Chapter 4

Problem Description and Proposed Solution

This chapter describes the considered problem and then presents the proposed solution for it.

4.1 Problem Definition

The objective of this thesis is to enable capturing hyperspectral images using cost effective and widely available lighting sources, including LED and CFL sources. However, as we showed in Chapter 3, such sources do not radiate enough power outside of the visible light range. Thus, hyperspectral bands in the non-visible range (which are the most useful) captured using these light sources suffer from substantial distortions, which renders them useless. This, in turn, severely limits the applicability of hyperspectral imaging in many practical applications.

The problem we address in this thesis is how to accurately restore damaged hyperspectral bands captured using LED and CFL light sources, instead of the expensive and often not available or not possible to use halogen light sources. This is a more general and more challenging problem than the RGB image restoration problem addressed in prior works for multiple reasons. In our problem, we need to concurrently restore many hyperspectral bands at once, compared to restoring one RGB image in prior works. Second, similar to RGB image restoration, the spatial accuracy needs to be ensured but for all bands. By spatial accuracy, we mean the similarity of the restored pixels to the ground truth ones in the x, y domain. Third, unlike RGB image restoration, the spectral accuracy must also be ensured in the case of hyperspectral band restoration. The spectral accuracy means the similarity of the restored pixels to the ground truth ones across the λ wavelength domain. The spectral accuracy is crucial because it impacts the accuracy of the spectral signatures created from the different bands, and spectral signatures are used for material identification and classification in hyperspectral applications.

4.2 Proposed Solution

We model our problem as band restoration which has some similarity with image restoration. Traditional approaches have been explored for denoising and restoring hyperspectral bands. Traditional methods do not work properly in this problem. Hyperspectral images are high dimensional data and multiple environmental factors such as illumination type, distance from the scene, and exposure time can result in various effects appearing in the images. Traditional non learning based works are not able to recover all possible disturbances as they mainly assume fixed conditions for the input data. However, Deep learning has been successful in recent years in addressing the image restoration problem, as well as others. We propose a deep neural networks as a solution for the hyperspectral band restoration problem. We design a neural network model that considers both the spatial and spectral domains. The proposed model is general and supports restoring different number of hyperspectral bands, which is a significant feature since the number of bands captured by hyperspectral cameras depends on the design of each camera, and it varies from one manufacturer to another, and even across models from the same manufacturer. In addition, we propose four loss functions and integrate them into the neural network model to maximize the spectral and the spatial accuracy across many hyperspectral bands.

In the following, we present the details of the neural network design and the loss functions.

4.2.1 Architecture of the Neural Network

The proposed network architecture is illustrated in Figure 4.1. Similar to previous models, e.g., [38, 37], we design our network using residual blocks (RBs) as the main element of the model. As shown in the figure, in addition to convolution (C), batch normalization (B) and ReLU activation (R) layers, each residual block has a skip connection from the input to the output of the bock. Batch normalization makes layer's input in each batch consistent, and ReLU activation keeps the network from the vanishing gradient problem, which results in helping the learning process of the network be steady and faster. Skip connections allow retaining some information from earlier layers, which helps in restoring damaged bands. Residual learning strikes a balance between remembering information from earlier layers and replacing it with new information from the later layers. The initial layers in a neural network contain low-level features and later layers have high-level features. Also, noise is usually dominant at high frequencies which disturbs images. However, there are some useful features at these high frequencies in noisy images such as edges of different objects (e.g., healthy vs defective apple) in different bands. Residual networks help in learning this useful information along with the elimination of existing noise. The proposed network has 10 residual blocks coming after a convolutional layer applied to the input for feature extraction, each has 6 layers. At the end of the network, there is a convolutional layer coming after a

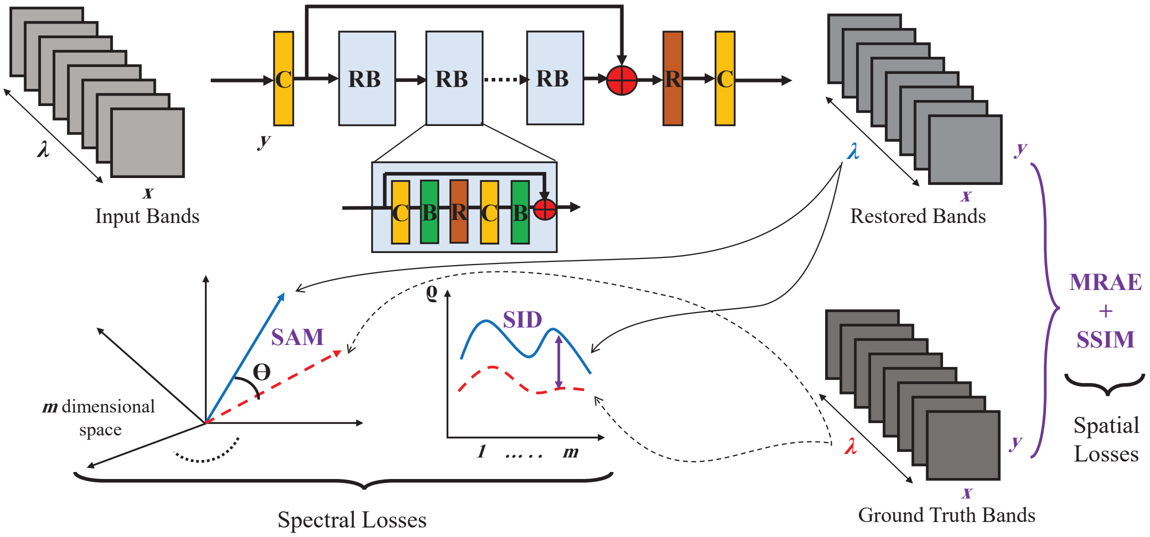

Figure 4.1: Network architecture of the proposed model. "C" = convolution, "R" = ReLU activation function, and "B" = Batch Normalization, respectively. "RB" denotes residual block, which is further expanded in the figure. Four loss functions, MRAE, MS-SSIM, SAM, and SID, are used to improve the accuracy of the restored bands in the spatial and spectral domains.

ReLU layer. The network is designed and trained on patches of images. The network does not change the spatial size of input and output images, resulting from using a stride of 1 in all convolution layers.

4.2.2 Loss Functions

Compared to RGB images, hyperspectral images have 3 dimensions. Our captured hyperspectral images, for instance, have 512 x 512 x 204 pixels. Thus, it is essential to consider both the spatial and spectral domains in our solution. To restore hyperspectral bands and ensure the accuracy of the both domains, we propose four loss functions, which are added linearly to make the final loss functions. The integration of these functions in the neural network model is shown in Figure 4.1. In the following, we define each loss function and justify its usage.

- **Mean Relative Absolute Error (MRAE):** One of the challenges in hyperspectral images is that the level of luminance varies across bands, especially when captured with LED and CFL light sources. This means that the values of pixels in some bands are higher than others. This can introduce bias towards bands with higher values. Thus, we propose using the mean relative absolute error as one of the losses in the network, which is defined as follows:

$$MRAE = \frac{1}{N} \sum_{i} \sum_{n} \left| \frac{I_{out}(i, \lambda_n) - I_{gt}(i, \lambda_n)}{I_{gt}(i, \lambda_n)} \right|,$$

where $I_{out}(i, \lambda_n)$ and $I_{gt}(i, \lambda_n)$ are values of i-th pixel at the n-th band of the output and ground truth images, and N is the total number of pixels in each image.

- **Multiscale Structural-similarity (MS-SSIM):** This is a perceptual loss defined to keep the shape and structure of the restored bands as close as possible to the ground truth. This loss function was introduced by Snell et al. [40] for learning tasks since it is differentiable. $L_{MS-SSIM}(I_{gt}, I_{out})$ is defined as:

  $$L_{MS\text{-}SSIM}(I_{gt}, I_{out}) = -\textstyle\sum_n \sum_i MS\text{-}SSIM(I_{out}(i, \lambda_n), I_{gt}(i, \lambda_n)),$$

  where

  $$MS\text{-}SSIM(x, \hat{x}) = I_M(x, \hat{x})^{\alpha_M} \prod_{j=1}^{M} C_j(x, \hat{x})^{\beta_j} S_j(x, \hat{x})^{\gamma_j},$$

  and M is a downsampling factor usually set to 5, and $H(x, \hat{x})$, $C(x, \hat{x})$, and $S(x, \hat{x})$ are defined as:

  $$H(x, \hat{x}) = \frac{2\mu_x \mu_{\hat{x}} + C_1}{\mu_x^2 + \mu_{\hat{x}}^2 + C1}, \qquad C(x, \hat{x}) = \frac{2\sigma_x \sigma_{\hat{x}} + C_2}{\sigma_x^2 + \sigma_{\hat{x}}^2 + C_2},$$

  $$S(x, \hat{x}) = \frac{2\sigma_{x\hat{x}} \sigma_{x\hat{x}} + C_3}{\sigma_x^2 + \sigma_{\hat{x}}^2 + C_3}.$$

  The variables μ_x,$\mu_{\hat{x}}$, σ_x, and $\sigma_{\hat{x}}$ are the mean and the standard deviations of pixel intensity in an image patch positioned at either x or $\hat{x}$, and C_1, C_2, and C_3 are constants.

- **Spectral Angle Matching (SAM):** SAM is a metric that measures the similarity between two spectra [23]. SAM considers each spectra as a vector with the number of bands as its dimension. We define a loss function based on this metric. This loss function tries to minimize the angle between two given vectors, which represent the reconstructed and ground truth bands. In other words, the value of the same pixel in all bands of a hyperspectral image form a vector, and the SAM loss function uses the dot product of the normalized versions of these vectors. Therefore, this loss function is not sensitive to the length of the vectors, while the angle between them is important. This feature helps the network to be robust against changes in the luminance level. The SAM loss function is defined as:

  $$SAM = \sum_{x,y} cos^{-1} \left(\frac{\overrightarrow{I_{out}}(i, \lambda_{1:m})}{\left|\left|\overrightarrow{I_{out}}(i, \lambda_{1:m})\right|\right|} \cdot \frac{\overrightarrow{I_{gt}}(i, \lambda_{1:m})}{\left|\left|\overrightarrow{I_{gt}}(i, \lambda_{1:m})\right|\right|} \right),$$

where $I_{out}(i, \lambda_{1:m})$ and $I_{gt}(i, \lambda_{1:m})$ are the spectral vectors with size m of the i-th pixel.

- **Spectral Information Divergence (SID):** The SAM metric treats spectral signatures as geometrical vectors, while the SID metric proposed by Chang [6] looks at them as random variables. SID, thus, considers the probabilistic differences between the probability distributions of the spectral signatures. We define a loss function using SID, which directs the spectral signature produced by the network to have a similar probabilistic behavior as the ground truth. We used the softmax function to transfer spectral signatures to the probability domain before using this loss function. The SID loss function is given by:

  $$SID \quad = \quad \sum_i [D(I_{out}(i, \lambda_{1:m}) \,||\, I_{gt}(i, \lambda_{1:m})) + D(I_{gt}(i, \lambda_{1:m}) \,||\, I_{out}(i, \lambda_{1:m}))]$$

  where:

  $$D(I_{out}(i, \lambda_{1:m}) \,||\, I_{gt}(i, \lambda_{1:m})) \quad = \sum_n I_{out}(i, \lambda_n) \cdot log_2 \left[\frac{I_{out}(i,\lambda_n)}{Im_{gt}(i,\lambda_n)} \right]$$

  and:

  $$D(I_{gt}(i, \lambda_{1:m}) \,||\, I_{out}(i, \lambda_{1:m})) \quad = \sum_n I_{gt}(i, \lambda_n) \cdot log_2 \left[\frac{I_{gt}(i,\lambda_n)}{I_{out}(i,\lambda_n)} \right].$$

Chapter 5

Experimental Evaluation

In this chapter, we assess the performance of the proposed hyperspectral band restoration method and compare it against the closest work in the literature, using a diverse dataset of hyperspectral images collected under different illumination conditions.

5.1 Experimental Setup

Image Acquisition Setup. The image acquisition setup is shown in Figure 5.1. It consists of a hyperspectral camera facing towards an experimental table, where we put the object(s) to be captured. We created three different setups for capturing the same scene using three different light sources. We categorize our dataset into three groups having different illumination conditions: (i) illuminating the scene with 2 halogen light sources from both directions providing ideal illumination condition, and these images are used as ground truth for our model, (ii) illuminating the scene with one LED light source, and (iii) illuminating the scene with one fluorescent light source from different directions.

We used the Specim IQ hyperspectral camera for collecting the data. It is a line scanning camera with a built-in scanner. This camera works in the visible and near infrared ($400 - 1000nm$) spectral range with ∼3nm spectral resolution providing 204 bands. This camera operates by chargeable batteries and it has an internal storage to save the captured data. It also has a mini display to help in focusing and adjusting the camera lens before capturing and configuring the exposure time. Captured images are later transferred to a workstation for post processing using a software tool provided with the Specim IQ camera to visualize hyperspectral images.

Data Collection. To demonstrate the effectiveness of the proposed hyperspectral band restoration method, we consider two broad classes of hyperspectral applications: (i) food quality inspection and (ii) material identification and classification. We would like to show that our method restores the damaged hyperspectral bands, which would allow such applications to function under LED and CFL lighting sources. Since the setups of these applications would greatly vary based on the actual industrial environment, we focus on assessing the

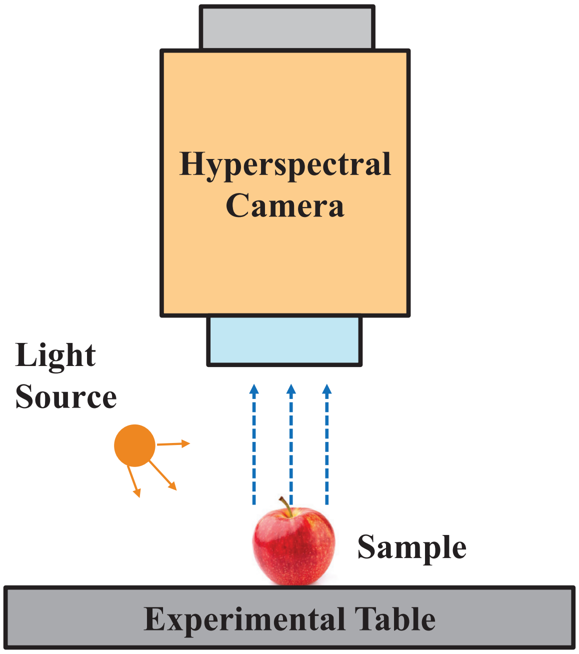

Figure 5.1: The experimental setup used to capture hyperspectral images under different illumination conditions.

quality of the restored bands and comparing them to the ground truth bands that are captured using ideal lighting conditions, which in this case are created using halogen light sources.

For the food quality inspection class of applications, we collected data for two fruit samples (apples and avocados) and meat samples (steak). Several previous studies proposed using hyperspectral imaging to investigate various issues in these common fruits, e.g., [29, 17], including determining ripeness and detecting bruises and internal defects. We purchased 15 samples of different apple types: 4 *honey crisp*, 4 *granny smith*, 2 *fuji*, 2 *gala*, and 3 *ambrosia*. We picked combinations of apples having different degrees of firmness and bruises.

To capture hyperspectral images of apples, we arranged the samples in groups of different sizes, ranging from 1 apple per group to 5 randomly chosen apples per group. For each group of apples, we captured at least one hyperspectral image, which contains 204 bands produced by the hyperspectral camera. We repeated the experiment for the considered three different light sources: halogen, LED, and CFL. In total, we captured 180 hyperspectral images of different types and groups of apples: 66 images were captured using halogen source, 57 using LED, and 57 using CFL. Similarly, we captured hyperspectral images of different types and groups of avocados. We had a total of 110 avocado hyperspectral images: 55 images were captured using halogen and 55 using CFL.

Also, we gathered hyperspectral images samples of steak with various thicknesses, different qualities and amount of fat captured in three different lighting. Hyperspectral imaging has been proposed for analyzing the nutrition and fat contents of meat and other foods, e.g., [19]. We captured a total of 186 steak hyperspectral images: 72 using halogen, 57 using CFL, and 57 under LED.

For the material identification class of applications, we collected data from different types of objects composed of various materials such as metal, wood, plastic, and paper. We captured objects individually and in groups. Thus, most scenes contained varieties of materials at the same time. In total, we captured a total of 123 hyperspectral images containing various objects: 49 using halogen, 49 using CFL, and 25 using LED. Figure 5.2 shows a few (RGB) samples of our datasets. And Table 5.1 summarizes the collected hyperspectral dataset, which we believe is unique in this domain and we make it publicly available at [1].

Table 5.1: Summary of the collected hyperspectral dataset. Each sample has 204 bands, where a band is 2d image

	Halogen	CFL	LED	Total
Apples	66	57	57	180
Avocado	55	55	-	110
Meat	72	57	57	186
Objects	49	49	25	123
Total	242	218	139	599

Figure 5.2: RGB samples from our dataset.

Model Implementation and Training. We implemented our neural network model using PyTorch. We used the Adam optimizer with a batch size of 64 and a decaying learning rate, and each convolutional layer has 64 filters with 3x3 size and a stride of 1. All training and testing of the model were done on a workstation with a NVIDIA TITAN RTX GPU.

We train our model for each class of applications separately. For example, for the material identification, we use the hyperspectral images collected from different objects, but we do not use images for fruits or meat. This is realistic, as such applications will not likely be mixed in the same environment and the characteristics of materials are quite different in each class, which makes using a single model to handle all such varieties impractical. For each application class, we divide the relevant dataset into three *disjoint* sets: training, validation, and testing.

For each sample in our dataset, we have three hyperspectral images: one taken under halogen, another under LED and a third under CFL. For training, we pair each image captured under CFL or LED with its corresponding image under halogen. The hyperspectral images taken under halogen light do not have distortions and are considered as the ground truth.

Each hyperspectral image has 204 bands. Since neighbouring bands are similar to each other and to save processing time, we selected 25 of these bands that are equally spaced in the spectral range. We note that our method is general and supports restoring any number of bands, including all of the 204 bands. Training on more bands will, however, take longer and require more memory. In practice, sample bands are typically used in hyperspectral applications.

We utilize common data augmentation techniques in the literature, including combinations of flipping and rotating the images. This augmentation has increased our datasets by 8 folds. In addition, our neural network model is designed to process patches of images. Each image is divided into 64 non-overlapping patches of size 50 x 50 pixels.

State-of-the-Art Compared Against. Our problem is close in nature to works that address noise reduction in hyperspectral imaging. We chose the most recent method for hyperspectral denoising [44] to compare against. This method, referred to as QRNN3D, was shown to outperform others in the literature. QRNN3D uses a recurrent neural network (RNN) with 3D convolutions to consider the spectral dimension in addition to the two spatial ones in the denoising process. QRNN3D was shown to handle different types of noise such as Gaussian noise, impulse noise, and dead pixels or lines. We trained QRNN3D on our datasets, in which hyperspectral bands contain noise due to diverse illumination conditions.

Performance Metrics. We use subjective and objective metrics in our analysis. We demonstrate multiple sample images from different bands and experiments to subjectively assess the visual quality and accuracy of our method relative to the ground truth and in comparison to the state-of-the-art. In addition, we show and compare sample spectral signatures across the entire spectrum.

We use five objective metrics to assess the spatial and spectral accuracies of the restored bands, relative to the ground truth. Four of these metrics are defined in Chapter 4 and they are: Mean Relative Absolute Error (MRAE), Structural Similarity Index Measure (SSIM), Spectral Angle Matching (SAM), and Spectral Information Divergence(SID). MRAE and

SSIM assess the spatial accuracy through measuring the error introduced in the restored bands as well as the similarity of their structure to the ground truth bands. SAM and SID consider the differences between the restored bands and the ground truth ones across the spectral dimension. The last metric is Coefficient of Correlation (CoC), which is commonly used in hyperspectral imaging works to measure how correlated are two spactras. The metric can be defined mathematically as follows:

$$CoC = \frac{\sum_n (I_{out}(i,\lambda_n) - \overline{I}_{out}(i,\lambda_n))(I_{gt}(i,\lambda_n) - \overline{I}_{gt}(i,\lambda_n))}{\sqrt{\sum_i (I_{out}(i,\lambda_n) - \overline{I}_{out}(i,\lambda_n))^2 (\sum_i I_{gt}(i,\lambda_n) - \overline{I}_{gt}(i,\lambda_n))^2}} \tag{5.1}$$

5.2 Results for Food Quality Inspection Applications

We present sample results showing the quality of the restored bands for hyperspectral applications designed for inspecting fruits such as apples. We start with the objective metrics, which are summarized in Table 5.2. All metrics reported in the table are measured relative to the ground truth. These metrics can be divided into two groups. The first group contains MRAE and SSIM, and it shows the quality of the restored images in the spatial domain. The second group measures the quality of the restored images in the spectral domain and contains SAM, SID, and CoC. it. As Table 5.2 shows, the proposed method outperforms the state-of-the-art across all metrics, and it produces fairly accurate bands across the spatial and spectral domains.

Table 5.2: Comparison of the proposed band restoration method against the state-of-the-art (QRNN3D) using multiple objective metrics. Data shown for the food quality inspection class of hyperspectral applications.

	Ours	QRNN3D	Comments
MRAE	**0.24694**	0.31486	Closer to 0 is better
CoC	**0.9170**	0.8040	Closer to 1 is better
SSIM	**0.84460**	0.64000	Closer to 1 is better
SAM	**0.05903**	0.18007	Closer to 0 is better
SID	**0.00013**	0.00015	Closer to 0 is better

Next, we present sample results to visually demonstrate the quality of the restored bands. Two samples are shown in Figure 5.4 and Figure 5.3 for different apples. Figure 5.4 shows the results for the CFL illumination setting, while Figure 5.3 shows the results for the LED illumination setting. In each figure, the RGB image is shown as well as four sample bands at wavelengths $740, 810, 890$, and $960nm$. The figures also show the ground truth bands captured using halogen illumination in the lowest row.

We can conclude three points from Figures 5.3 and 5.4. First, hyperspectral bands captured under LED and CFL illuminations (1st row) are severely damaged, especially for the most important bands in the infrared range. Second, the proposed band restoration method produces much better hyperspectral bands than the state-of-the-art (QRNN3D). Third, the bands produced by our method are close to the ground truth.

Finally, we analyze and compare the spectral signatures created based on bands restored by our method versus the ones restored by the state-of-the-art method. Figure 5.5 presents a sample of our results. The figure also shows the spectral signatures created from the ground truth bands and from the noisy inputs for comparison. The figure shows that signatures created based on bands produced by our method are much closer to the ground truth signatures than the ones produced by the state-of-the-art method.

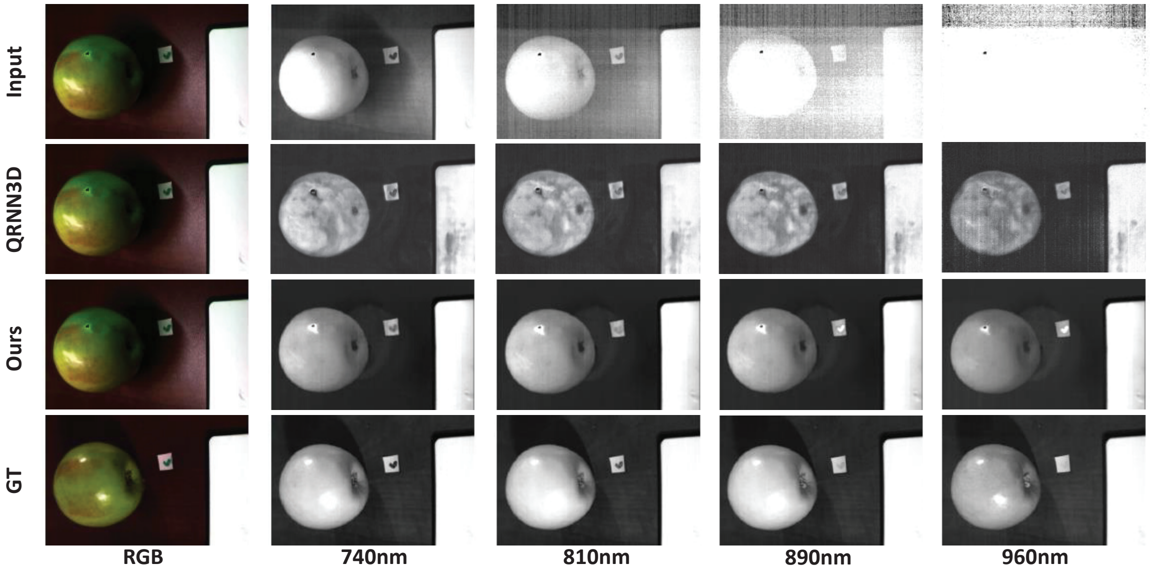

Figure 5.3: Comparison of the bands produced by the proposed method (3rd row) against the ground truth (4th row) and the state-of-the-art (2nd row) from the input data (1st row). Data shown for the LED illumination setting.

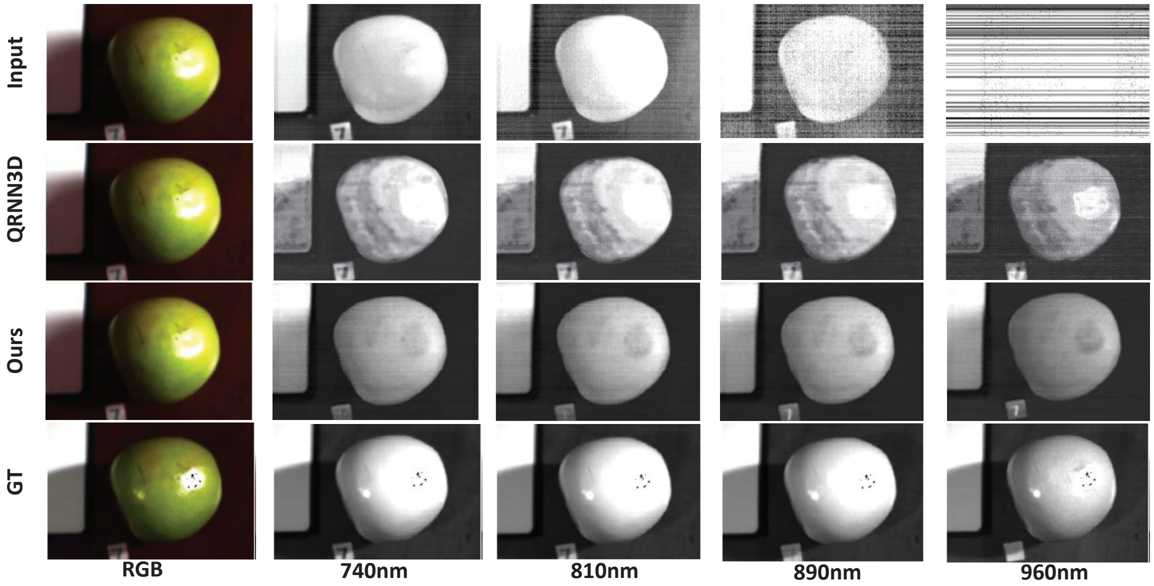

Figure 5.4: Comparison of the bands produced by the proposed method (3rd row) against the ground truth (4th row) and the state-of-the-art (2nd row) from the input data (1st row). Data shown for the CFL illumination setting.

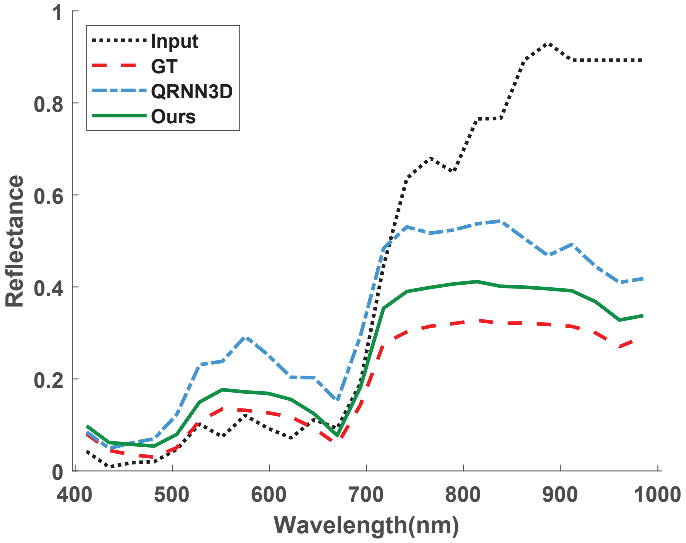

Figure 5.5: Spectral Signature for the apple in Figure 5.4.

5.3 Results for Material Identification Applications

We evaluate our method on another common class of hyperspectral imaging applications, which is material identification. As described in Section 5.1, we collected hyperspectral images of different materials. We trained our model on some (but not all) materials. That is, we intentionally put some objects in the test dataset that were not seen during the training process.

Two representative samples of our results are shown in Figure 5.6 for the CFL illumination condition and in Figure 5.7 for the LED illumination condition. We note that none of the images in the training set contained the cups in Figure 5.6 or the whiteboard markers in Figure 5.7. However, our network used the characteristics of other objects with similar materials in the training dataset to restore the hyperspectral bands of these objects that were never seen before.

In Figure 5.6, there are three cups. The white cup is made of paper and the blue and red cups are made of plastic. We show in Figure 5.8 the spectral signatures for the two different materials of the cups. The figure shows that our method produces fairly accurate signatures that are close to the ground truth ones. This is unlike the signatures created by the QRNN3D method, which deviate from the ground truth signatures, and hence may compromise the performance of hyperspectral systems used for material identification.

Finally, we present the summary of the objective performance metrics in Table 5.3, which shows that our method outperforms the state-of-the-art in all metrics. We note, however, that the performance of our method on this class of applications is relatively lower than its performance on the food quality inspection class of applications (summarized in Table 5.2). This is because our setup contained significantly more diverse objects and materials in the material identification case. In real-life applications, hyperspectral systems are typically designed to differentiate a smaller number of different materials, e.g., identifying metal objects from non-metal ones for recycling purposes. Thus, we expect our method to perform even better for real applications.

Table 5.3: Comparison of the proposed band restoration method against the state-of-the-art (QRNN3D) using multiple objective metrics. Data shown for the material identification class of hyperspectral applications.

	Ours	QRNN3D	Comments
MRAE	**0.39096**	0.48839	Closer to 0 is better
CoC	**0.8693**	0.7280	Closer to 1 is better
SSIM	**0.75140**	0.58540	Closer to 1 is better
SAM	**0.09199**	0.19367	Closer to 0 is better
SID	**0.00020**	0.00027	Closer to 0 is better

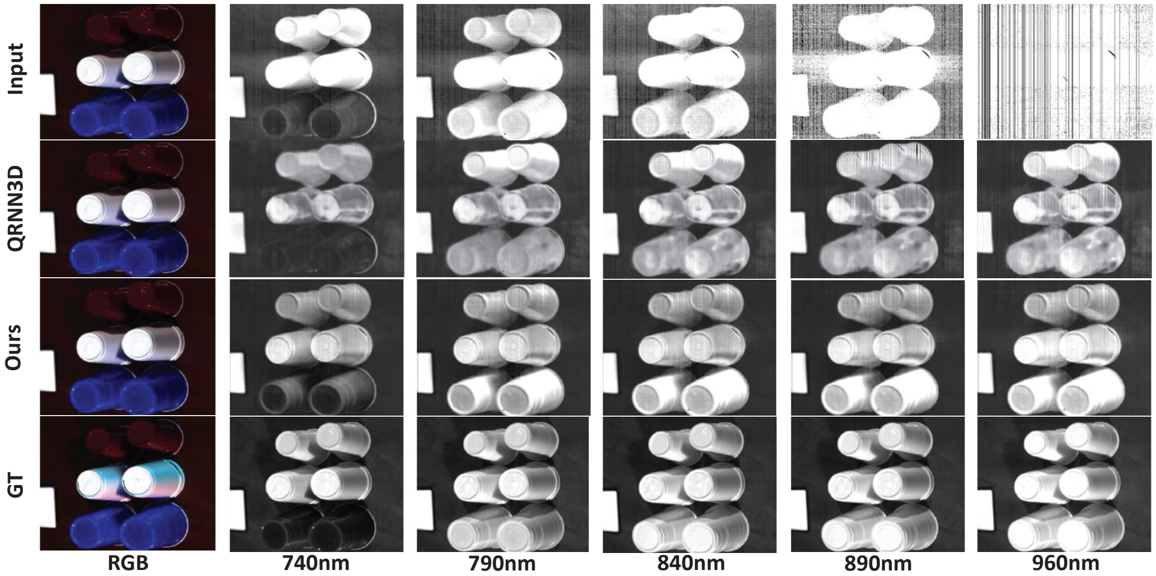

Figure 5.6: Comparison of the bands produced by the proposed method (3rd row) against the ground truth (4th row) and the state-of-the-art (2nd row) from the input data (1st row). Data shown for the CFL illumination setting.

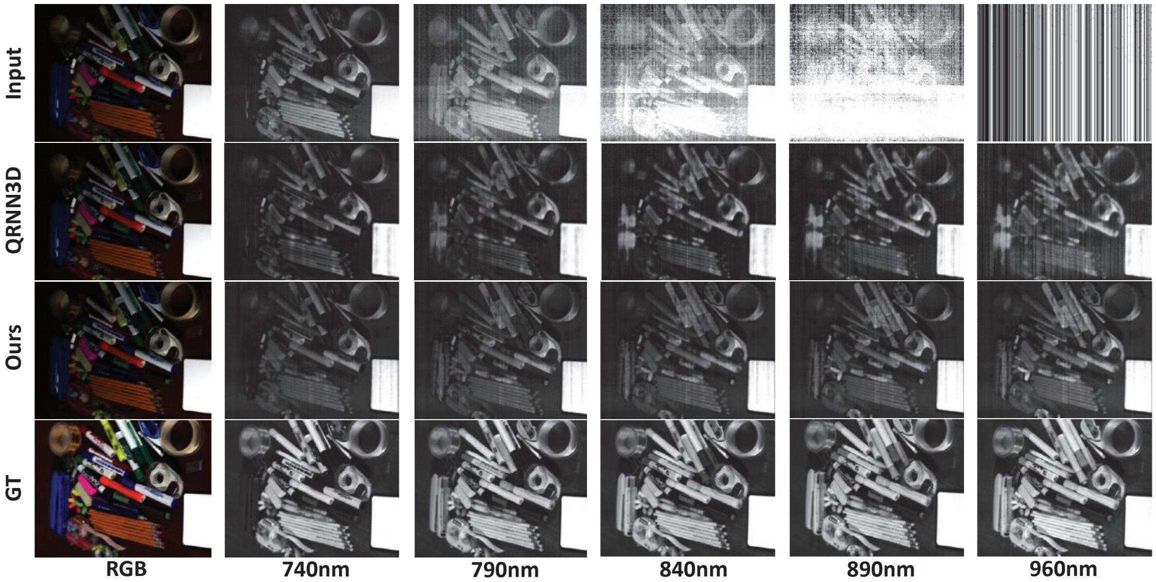

Figure 5.7: Comparison of the bands produced by the proposed method (3rd row) against the ground truth (4th row) and the state-of-the-art (2nd row) from the input data (1st row). Data shown for the LED illumination setting.

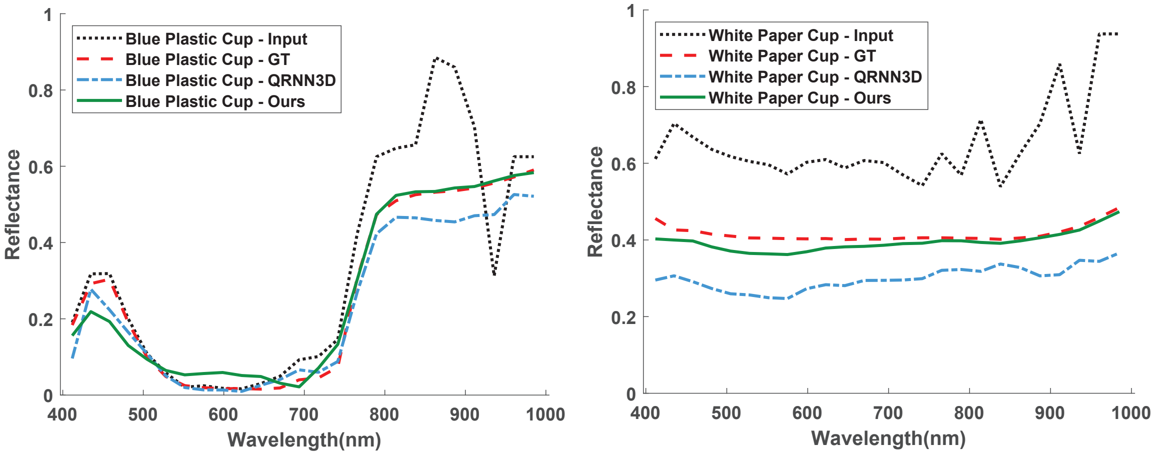

(a) (b)

Figure 5.8: Spectral Signature for objects in Figure 5.6.

5.4 Results for Real-life Images

We verify our proposed model by testing on hyperpsectral images captured indoor under diverse, uncontrolled, illumination scenarios outside of our labs. For this experiment, we have gathered samples of real-life hyperspectral images covering visible and near infrared range of the spectrum using the Specim IQ camera. We use the pretrained neural network for material identification application from section 5.3 and test this network on real world test data. We also test these data on QRNN3D model trained on the objects dataset in Section 5.3 in order to compare the ability of both netwroks in recovering the real world data. The visual quality results for three different scenes are shown in Figure 5.9. Our model successfully addresses these scenes captured under diverse illumination conditions. It results in images with considerably less artifacts than the produced images by the state-of-the-art. Consequently, it shows the proposed model's strength in handling uncontrolled illumination conditions. Our model is generalized due to several reasons; First, we utilized the most common efficient light sources in our dataset. Second, we included different scenarios such as lighting from different directions or capturing images with various exposure times. Third, the model is carefully designed based on spectral and spatial characteristics of hyperspectral images, and we also used Spectral Information Divergence in the proposed loss function, which makes the model able to handle the uncertainty existing in the damaged images. Finally, we enlarged the data by benefiting augmentation techniques and patch-based training.

Figure 5.9: Comparison of the produced bands by our proposed and QRNN3D netwroks for three different real life scenes.

5.5 Ablation Study

In order to analyze the impact of loss functions on proposed model, we conduct an ablation study. We train the neural network separately with the same settings and various loss functions to make it possible to compare their effects. At first, we use the Mean Square Error (MSE) which is one of the most popular reconstruction loss functions in training neural networks for computer vision tasks. Next, we train the network utilizing the proposed spectral loss. Then, we add the spatial loss, and we, finally, train the network using both spectral and spatial loss functions together. We present the test results of training the network using the food processing dataset in Table 5.4 in which MRAE and SAM respectively show the spatial and spectral reconstruction quality.

Table 5.4: Comparison of the various loss functions impact

	MSE	Spectral	Spatial	Spectral + Spatial	Comments
MRAE	0.72120	22.6749	0.27255	**0.25541**	Closer to 0 is better
SAM	0.17612	0.06503	0.08575	**0.06104**	Closer to 0 is better

Table 5.4 shows that using MSE can produce outputs neither with acceptable spatial nor with sufficient spectral quality. In this setting, the SAM metric is considerably lower compared to its value of using the proposed spectral loss function. MRAE is also significantly smaller when we benefit from the proposed spatial loss. This shows the importance of the effect of variations in the level of luminance across bands which MSE cannot handle.

However, using the spectral loss results in the worst MRAE in the table. This is because spectral loss function does not pay attention to the pixels values and it only considers the pattern of spectral signatures of the restored and ground truth images. Also, utilizing the spatial loss function is not able to provide the best spectral quality. Finally, training the networ on both the spectral and spatial loss functions outperforms all previous netwroks.

Chapter 6

Conclusions and Future Work

6.1 Conclusions

In this thesis, we considered the problem of capturing hyperspectral imaging using common lighting sources such as fluorescent (CFL) and light emitting diode (LED) for indoor applications, instead of using expensive, and occasionally not possible to use, halogen sources. Unlike halogen sources, CFL and LED light sources emit low power in the invisible range of the spectrum. We analyzed the effects of using different light sources on hyperspectral imaging and showed that CFL and LED sources introduce significant noises and damages in the hyperspectral bands in the invisible range of the spectrum, which are the most important bands for the applications. Then, we proposed a deep-learning model to restore the damaged hyperspectral bands, which accounts for the spatial and spectral characteristics of hyperspectral images. We collected a hyperspectral image dataset of around 600 images, each with 204 bands. Our dataset contains different objects and materials captured using various lighting sources. We are not aware of similar datasets in the literature. We conducted an empirical study to analyze the performance of the proposed method. Our results showed that the proposed method produces hyperspectral bands that are close to the ground truth bands captured under ideal illumination conditions. Thus, the proposed method could facilitate the deployment of hyperspectral imaging systems for many real-life applications using cost-effective lighting sources. In addition, we compared the proposed method against the closest work in the literature, using multiple objective and subjective metrics. Our results showed that the proposed method outperforms the state-of-the-art across all metrics. Finally, our method results in a considerable amount of power-saving compared to using halogen light sources while capturing hyperspectral images in industrial locations such as warehouses.

6.2 Future Work

The work in this thesis can be extended in multiple directions. For example, the deep learning model can be implemented on the hyperspectral camera itself. Current hyperspectral cameras have GPU in their system. For example, Specim IQ uses NVIDIA Tegra K1. The GPUs are on the hyperspectral cameras are currently utilized for various tasks such as classification of hyperspectral images. Optimizing the proposed model for implementation on the camera hardware and integrating it with the current pipeline can lead to more powerful and versatile hyperspectral cameras that could be used used for more real-life applications, especially the ones that require fast or real-time processing. Another direction for extending this work is exploring potential application of hyperspectral applications, such as artworks authentication. Current approaches for validating artworks are invasive and destructive, which can result in damages to the artworks. Using hyperspectral images is an alternative approach for this application. However, halogen light sources can cause harm to the artworks too. The work done in this thesis can be a solution without any potential damages to these valuable items. Extending this work for this application requires gathering relevant datasets to this problem. Next, the proposed band restoration method can be adapted to support outdoor applications, especially for mitigating the effect of weather conditions on hyperspectral images since illumination conditions similarly vary in adverse climate conditions, and introduce noises in captured images. Finally, the proposed method can be explored for applying to the applications requiring bands above near-infrared (NIR) including part of short wave infrared (SWIR); however, it may not be able to work for higher wavelengths such as far-infrared (FIR).

Bibliography

[1] Dataset and source code. `https://github.com/pazadimo/HS_In_Diverse_Illuminations`, 2021.

[2] Mohammad Amin Arab, Puria Azadi Moghadam, Mohamed Hussein, Wael Abd-Almageed, and Mohamed Hefeeda. Revealing true identity: Detecting makeup attacks in face-based biometric systems. In *Proc. of ACM Conference on Multimedia (MM'20)*, page 3568–3576, Seattle, WA, October 2020.

[3] Puria Azadi Moghadam, Neha Sharma, and Mohamed Hefeeda. Enabling hyperspectral imaging in diverse illumination conditions for indoor applications. In *Proc. of ACM Multimedia Systems Conference(MMSys'21)*, Istanbul, Turkey, September 2021.

[4] Seung-Hwan Baek, Incheol Kim, Diego Gutierrez, and Min H. Kim. Compact single-shot hyperspectral imaging using a prism. *ACM Transaction on Graphics*, 36(6), November 2017.

[5] Marcus Borengasser, William S Hungate, and Russell Watkins. *Hyperspectral Remote Sensing: Principles and Applications*. CRC press, 2007.

[6] Chein-I Chang. An information-theoretic approach to spectral variability, similarity, and discrimination for hyperspectral image analysis. *IEEE Transactions on Information Theory*, 46(5):1927–1932, 2000.

[7] Xiaochuan Chen, Mark S Drew, and Ze-Nian Li. Illumination and reflectance spectra separation of hyperspectral image data under multiple illumination conditions. *Electronic Imaging*, 2017(18):194–199, 2017.

[8] Costanza Cucci and Andrea Casini. Chapter 3.8 - hyperspectral imaging for artworks investigation. In José Manuel Amigo, editor, *Hyperspectral Imaging*, volume 32 of *Data Handling in Science and Technology*, pages 583–604. Elsevier, 2020.

[9] Danilo Ferreira de Souza, Pedro Paulo Fernandes da Silva, Luiz Fernando Almeida Fontenele, Gunther Damaceno Barbosa, and Marcelo de Oliveira Jesus. Efficiency, quality, and environmental impacts: A comparative study of residential artificial lighting. *Energy Reports*, 5:409 – 424, 2019.

[10] Peijun Du, Xiaomei Wang, Kun Tan, and G. Foody. Impacts of noise on the accuracy of hyperspectral image classification by svm. 2008.

[11] Gerda Edelman, Ton G. van Leeuwen, and Maurice C.G. Aalders. Hyperspectral imaging for the age estimation of blood stains at the crime scene. *Forensic Science International*, 223:72 – 77, 2012.

[12] Gamal Elmasry, Mohammed Kamruzzaman, Da-Wen Sun, and Paul Allen. Principles and applications of hyperspectral imaging in quality evaluation of agro-food products: A review. *Critical Reviews in Food Science and Nutrition*, 52(11):999–1023, 2012.

[13] C. Elvidge, D. V. Keith, B. Tuttle, and K. Baugh. Spectral identification of lighting type and character. *Sensors (Basel, Switzerland)*, 10:3961 – 3988, 2010.

[14] Y. Fu, Y. Zheng, L. Zhang, and H. Huang. Spectral reflectance recovery from a single rgb image. *IEEE Transactions on Computational Imaging*, 4(3):382–394, 2018.

[15] B. J. Fubara, M. Sedky, and D. Dyke. Rgb to spectral reconstruction via learned basis functions and weights. In *Proc. of IEEE Conference on Computer Vision and Pattern Recognition Workshops (CVPRW'20)*, pages 1984–1993, Seattle, WA, June 2020.

[16] Elham Kordi Ghasrodashti, Azam Karami, Rob Heylen, and Paul Scheunders. Spatial resolution enhancement of hyperspectral images using spectral unmixing and bayesian sparse representation. *Remote Sensing*, 9(6):541, 2017.

[17] D. Girod, J. A. Landry, G. Doyon, J. A. Osuna-Garcia, S. Salazar-Garcia, and R. Geonaga. Evaluating hass avocado maturity using hyperspectral imaging. In *Proc. of the Caribbean Food Crops Society*, Miami, FL, August 2008.

[18] X. Han, B. Shi, and Y. Zheng. Residual hsrcnn: Residual hyper-spectral reconstruction cnn from an rgb image. In *Proc. of International Conference on Pattern Recognition (ICPR'18)*, pages 2664–2669, Beijing, China, August 2018.

[19] Mohammed Kamruzzaman, Gamal ElMasry, Da-Wen Sun, and Paul Allen. Non-destructive prediction and visualization of chemical composition in lamb meat using nir hyperspectral imaging and multivariate regression. *Innovative Food Science & Emerging Technologies*, 16:218–226, 2012.

[20] A. C. Karaca, A. Ertürk, M. K. Güllü, M. Elmas, and S. Ertürk. Analysis of evidence in forensic documents using hyperspectral imaging system. In *Proc. of Signal Processing and Communications Applications Conference (SIU'12)*, pages 1–4, Istanbul, Turkey, October 2012.

[21] Shawn C Kefauver, Josep Peñuelas, and Susan L Ustin. Applications of hyperspectral remote sensing and gis for assessing forest health and air pollution. In *Proc. of IEEE International Geoscience and Remote Sensing Symposium*, pages 3379–3382, 2012.

[22] Zohaib Khan. Hyperspectral imaging and analysis for sparse reconstruction and recognition, 2014.

[23] F.A. Kruse, A.B. Lefkoff, J.W. Boardman, K.B. Heidebrecht, A.T. Shapiro, P.J. Barloon, and A.F.H. Goetz. The spectral image processing system (sips)—interactive visualization and analysis of imaging spectrometer data. *Remote Sensing of Environment*, 44(2):145 – 163, 1993.

[24] C. Lanaras, E. Baltsavias, and K. Schindler. Hyperspectral super-resolution by coupled spectral unmixing. In *Proc. of IEEE International Conference on Computer Vision (ICCV'15)*, pages 3586–3594, Santiago, Chile, December 2015.

[25] V. Lempitsky, A. Vedaldi, and D. Ulyanov. Deep image prior. In *Proc. of IEEE Conference on Computer Vision and Pattern Recognition(CVPR'18)*, pages 9446–9454, Salt Lake City, UT, June 2018.

[26] Wenjing Lv and Xiaofei Wang. Overview of hyperspectral image classification. *Journal of Sensors*, 2020.

[27] Marena Manley. Near-infrared spectroscopy and hyperspectral imaging: non-destructive analysis of biological materials. *Chemical Society Reviews*, 43(24):8200–8214, 2014.

[28] Federico Marini and José Manuel Amigo. Chapter 2.4 - unsupervised exploration of hyperspectral and multispectral images. In José Manuel Amigo, editor, *Hyperspectral Imaging*, volume 32 of *Data Handling in Science and Technology*, pages 93–114. Elsevier, 2020.

[29] Patrick M Mehl, Yud-Ren Chen, Moon S Kim, and Diane E Chan. Development of hyperspectral imaging technique for the detection of apple surface defects and contaminations. *Journal of Food Engineering*, 61(1):67–81, 2004.

[30] Andrei Nardelli, Eduardo Deuschle, Leticia Dalpaz de Azevedo, João Lorenço Novaes Pessoa, and Enedir Ghisi. Assessment of light emitting diodes technology for general lighting: A critical review. *Renewable and Sustainable Energy Reviews*, 75:368–379, 2017.

[31] Adam Polak, Timothy Kelman, Paul Murray, Stephen Marshall, David J.M. Stothard, Nicholas Eastaugh, and Francis Eastaugh. Hyperspectral imaging combined with data classification techniques as an aid for artwork authentication. *Journal of Cultural Heritage*, 26:1 – 11, 2017.

[32] Marco AC Potenza, Daniele Nazzari, Llorenç Cremonesi, Ilaria Denti, and Paolo Milani. Hyperspectral imaging with deformable gratings fabricated with metal-elastomer nanocomposites. *Review of Scientific Instruments*, 88(11), 2017.

[33] Behnood Rasti, Paul Scheunders, Pedram Ghamisi, Giorgio Licciardi, and Jocelyn Chanussot. Noise reduction in hyperspectral imagery: Overview and application. *Remote Sensing*, 10(3):482, 2018.

[34] J. Schanda. Instrumentation | photometry. In Robert D. Guenther, editor, *Encyclopedia of Modern Optics*, pages 307–317. Elsevier, Oxford, 2005.

[35] Stefano Selci. The future of hyperspectral imaging. *Journal of Imaging*, 5(11), 2019.

[36] Osram Opto Semiconductors. Life cycle assessment of illuminants—a comparison of light bulbs, compact fluorescent lamps and led lamps. *OsramOpto Semiconductors GmbH*, 2009.

[37] Neha Sharma and Mohamed Hefeeda. Hyperspectral reconstruction from rgb images for vein visualization. In *Proc. of ACM Multimedia Systems Conference(MMSys'20)*, page 77–87, Istanbul, Turkey, June 2020.

[38] Z. Shi, C. Chen, Z. Xiong, D. Liu, and F. Wu. Hscnn+: Advanced cnn-based hyperspectral recovery from rgb images. In *Proc. of IEEE Conference on Computer Vision and Pattern Recognition Workshops(CVPRW'18)*, pages 1052–10528, Salt Lake City, UT, June 2018.

[39] O. Sidorov and J. Y. Hardeberg. Deep hyperspectral prior: Single-image denoising, inpainting, super-resolution. In *Proc. of IEEE International Conference on Computer Vision Workshop (ICCVW'19)*, pages 3844–3851, Seoul, Korea (South), October 2019.

[40] J. Snell, K. Ridgeway, R. Liao, B. D. Roads, M. C. Mozer, and R. S. Zemel. Learning to generate images with perceptual similarity metrics. In *Proc. of IEEE International Conference on Image Processing (ICIP'17)*, pages 4277–4281, Beijing, China, September 2017.

[41] Petra Tatzer, Markus Wolf, and Thomas Panner. Industrial application for inline material sorting using hyperspectral imaging in the nir range. *Real-Time Imaging*, 11(2):99–107, 2005.

[42] B. Uzkent, M. J. Hoffman, and A. Vodacek. Real-time vehicle tracking in aerial video using hyperspectral features. *Proc. of IEEE Conference on Computer Vision and Pattern Recognition Workshops (CVPRW'16)*, pages 1443–1451, July 2016.

[43] Nan-Nan Wang, Da-Wen Sun, Yi-Chao Yang, Hongbin Pu, and Zhiwei Zhu. Recent advances in the application of hyperspectral imaging for evaluating fruit quality. *Food analytical methods*, 9(1):178–191, 2016.

[44] K. Wei, Y. Fu, and H. Huang. 3-d quasi-recurrent neural network for hyperspectral image denoising. *IEEE Transactions on Neural Networks and Learning Systems*, 32(1):363–375, 2021.

[45] Di Wu and Da-Wen Sun. Advanced applications of hyperspectral imaging technology for food quality and safety analysis and assessment: A review—part i: Fundamentals. *Innovative Food Science & Emerging Technologies*, 19:1–14, 2013.

[46] Hongyan Zhu, Bingquan Chu, Yangyang Fan, Xiaoya Tao, Wenxin Yin, and Yong He. Hyperspectral imaging for predicting the internal quality of kiwifruits based on variable selection algorithms and chemometric models. *Scientific Reports*, 7(1):1–13, 2017.

Appendix A

Dataset and Source Code Description

This appendix contains information about how to install the requirements for running the code to train the proposed neural network and to reproduce the results obtained in this thesis. The code and dataset for training, validation and testing are publicly available. We note that the paper published based on this thesis work [3] has received the reproducibility badge from the ACM Multimedia Systems 2021 Conference.

A.1 Code and Datasets

A.1.1 Obtaining and Installing the Code

The code can be found on GitHub at `https://github.com/pazadimo/HS_In_Diverse_Illuminations`

Use:

```
$ git clone https://github.com/pazadimo/HS_In_Diverse_Illuminations.git
```

```
$ cd HS_In_Diverse_Illuminations
```

Install PyTorch and other dependencies. For Conda users, you can create a new Conda environment using:

```
$ conda env create -f environment.yml
$ conda activate HSIDI
```

A.1.2 Hardware dependencies

To run the train and test code for the provided neural network, you need a NVIDIA GPU supporting CUDA.

A.1.3 Software dependencies

The main requirements are:

- Python 3.7.7
- MATLAB
- Pytorch 1.5.0
- CUDA CuDNN

A.1.4 Dataset

The provided dataset is divided into training, validation, and testing sets and covers two hyperspectral imaging applications including fruit processing and material identification. The publicly avalaible dataset contains 25 bands from 400nm to 1000nm. The complete dataset has 204 bands from 400nm to 1000nm for each hyperspectral image which can be available upon request due to large size.

Dataset is available at https://drive.google.com/drive/folders/18Q-iWels4sZxSrVmne7HgXMM3pKkQCTM?usp=sharing

A.2 Experiment Workflow

A.2.1 Training

Training dataset preparation:

- Original augmented dataset in .mat format for the Food Processing(FP) and Material Identification(MI) categories is available at following links:
  -**FP**: https://drive.google.com/drive/folders/1BI6J3aJiuqpXMFlNwYt3O0JLP3PHW4zD?usp=sharing
  -**MI**: https://drive.google.com/drive/folders/1LBvEqoJuQ3o9ryulqWbktEmI3K-g-K_1?usp=sharing
- The model requires 50x50x25 patches sampled from augmented dataset for the training process stroed in .h5 format.

- Training and Validation .h5 files for the both fruit processing and material identification categories are available at follwing links which you need to download them for training the model:
  - **FP Training Set**: https://drive.google.com/file/d/1qQGmerp7RU6igRSg7gUWX62EvTj1YYsS/view?usp=sharing
  - **FP Validation set**: https://drive.google.com/file/d/1EvY3f-Rbm2FYMmw7SWA30pbO4WyTWXqz/view?usp=sharing

  - **MI Training Set**: https://drive.google.com/file/d/1fhotXS85J7Bt1oH8AHxa4zNt9fon1wJt/view?usp=sharing
  - **MI Validation set**: https://drive.google.com/file/d/1_hZJZIYA2yI0v2WRkpIFpur6ae8ldCup/view?usp=sharing
- Move these downloaded .h5 files to *./train/Data/* directory.

Train the models:

- Train a model for the fruit processing application:

```
$ python train_fruit.py
```

- Train a model for the material identification application:

```
$ python train_material.py
```

- The trained models will be stored in *./train/models/* folder with log files.

A.2.2 Reproducing our Results

Test dataset preparation:

- Test Dataset for both Fruit Processing and Material Identification Applications is available at:
  - Test Data: https://drive.google.com/file/d/1a3R77JJvedsuCH8KoR_m5H_BOaw62fA1/view?usp=sharing
- Extract *Data.zip* file and transfer resulted *Data* folder into *./test/* directory.

Test the models:

- The pre-trained models for both applications are present in *./test/models/* folder. Follow the next steps to get exact numerical and visual results as the evaluation chapter.

- Test pre-trained model for fruit processing application by using the following code in *./test/* directory.

```
$ python evaluate_model_fruit.py
```

- Test pre-trained model for material identification application by using the following code in *./test/* directory.

```
$ python evaluate_model_material.py
```

- By running each of these files, the value of MRAE, SAM, and SID metrics for the resulted hyperspectral images of the test sets will be printed.
- Resulted Images are available in *./test/Data/Fruit/test_results* and *./test/Data/Material/test_results* in .mat format. You can analyze them using matlab.
- For visualizing the inputs, ground truth, and resulted images of the same scenes shown in the evaluation chapter, run this MATLAB file: *./test/visualize.m* It will visualize bands number 15, 17, 19, 21, and 24 ($\sim$ 740, 790, 840, 890, and 960nm) and also saves figures in .png format in *./test/* directory.